Ice fog observed at cirrus temperatures at Dome C, Antarctic Plateau

Étienne Vignon[1], Lea Raillard[1], Christophe Genthon[1], Massimo Del Guasta[2], Andrew J. Heymsfield[3], Jean-Baptiste Madeleine[1], and Alexis Berne[4]

[1]Laboratoire de Météorologie Dynamique/IPSL/Sorbonne Université/CNRS, UMR 8539, Paris, France
[2]INO-CNR, Sesto Fiorentino, Italy
[3]National Center for Atmospheric Research, Boulder, Colorado
[4]Environmental Remote Sensing Laboratory (LTE), École Polytechnique Fédérale de Lausanne, Switzerland

Correspondence: É. Vignon (etienne.vignon@lmd.ipsl.fr)

Abstract.

As the near-surface atmosphere over the Antarctic Plateau is cold and pristine, its physico-chemical conditions resemble to a certain extent those of the high-troposphere where cirrus clouds form. In this paper, we carry out an observational analysis of two shallow fog clouds forming in-situ at cirrus-temperatures - that is, temperatures lower than 235 K - at Dome C, inner Antarctic Plateau. The combination of lidar profiles with temperature and humidity measurements from advanced thermo-hygrometers along a 45-m mast makes it possible to characterise the formation and development of the fog. High supersaturations with respect to ice are observed before the initiation of fog and the values attained suggest that the nucleation process at play is the homogeneous freezing of solution aerosol droplets. This is the first time that in situ observations show that this nucleation pathway can be at the origin of an ice fog. Once nucleation occurs, the relative humidity gradually decreases down to subsaturated values with respect to ice in a few hours, likely owing to vapour deposition onto ice crystals and turbulent mixing. The development of fog is tightly coupled with the dynamics of the boundary-layer which, in the first study case, experiences a weak diurnal cycle while in the second case, transits from a very stable to a weakly stable dynamical regime. Overall, this paper highlights the potential of the site of Dome C for carrying out observational studies of cloud microphysical processes in natural conditions and using in-situ ground-based instruments.

1 Introduction

Given the prevailing very cold temperatures and the pristine air, the near-surface atmosphere over the Antarctic Plateau shares similarities with the high-troposphere in terms of physico-chemical conditions. Antarctic ice fogs, i.e. near-surface ice clouds, have been observed at typical cirrus temperatures namely $T < 235$ K (Ricaud et al., 2017), and it is therefore legitimate to question to what extent their microphysical properties resemble those of cirrus clouds. Ice fogs have non-negligible effects on polar climates as their radiative forcing has significant impacts on the surface energy budget (e.g. Blanchet and Girard, 1995). Ice fogs can be distinguished from another surface ice cloud type called 'diamond dust' through visibility criteria - fogs are optically deeper - or ice crystal properties. For instance, Girard and Blanchet (2001) distinguish ice fog from diamond dust by

the high concentration of ice crystals of small diameters as the particles' number concentration in fog clouds generally exceeds 1000 L^{-1} and their size is below 30 μm. As stressed in Gultepe et al. (2017), this classification is nonetheless subjective and the distinction between ice fogs and diamond dust is somewhat blurred. In the present paper, we use the term 'ice fogs' independently for fog and diamond dust.

Most of polar ice fogs have a liquid-origin and form through the advection of warm and moist air from the mid-latitudes followed by radiative cooling (e.g. Curry et al., 1990). The formation of fog is also generally pre-conditioned and accompanied by a stable stratification in the boundary layer (Gultepe et al., 2015) which maintains the humidity and the low temperatures near the surface. Gultepe et al. (2017) summarise the microphysical and dynamical processes through which liquid-origin ice fogs develop. Liquid-origin ice fog crystals form by either homogeneous or heterogeneous nucleation. In the former case, supercooled liquid droplets produced at higher temperatures through Cloud Condensation Nuclei (CCN) activation, - e.g. above the open ocean - are advected into a colder environment - e.g. above a continental surface, the sea-ice or an ice-sheet - and then freeze when T < 235 K. In the second case, supercooled water droplets can freeze at higher temperature if they contain or enter in contact with Ice Nuclei Particles (INPs). In addition to these so-called immersion and contact freezing processes, heterogeneous nucleation might occur without the presence of supercooled liquid droplets through the direct deposition of water vapor onto INPs but the occurrence of such a process in the atmosphere is still debated (Marcolli, 2014). Given the low concentrations of INPs over the Antarctic (Belosi et al., 2014), supercooled liquid droplets have been observed at very cold temperatures down to 240 K (Silber et al., 2019; Ricaud et al., 2020; Rowe et al., 2022) and they were shown to be at the origin of fogs over the Antarctic coast (Kikuchi, 1971, 1972).

Ice fogs forming locally over the Antarctic Plateau when the temperature remains well below 235 K have received much less attention. In this cirrus-temperature regime, no supercooled water droplets are present and the fog necessarily cannot have a liquid origin. In this particular case, ice crystals may form through freezing of solution aerosol particles also named haze droplets (Heymsfield and Sabin, 1989; Girard and Blanchet, 2001) when the relative humidity reaches a value that depends on the particle size and water activity. This value is above the saturation with respect to ice - so the air is supersaturated with respect to ice - but is lower than the liquid water saturation (Koop et al., 2000; Baumgartner et al., 2022). There is also evidence that solution aerosol particles can also freeze heterogeneously due to the presence of INPs (DeMott et al., 1998; Kärcher and Lohmann, 2003) but this process remains poorly understood especially at very low temperatures (Heymsfield et al., 2017).

The air near the surface of the Antarctic Plateau frequently experiences high supersaturations with respect to ice (Genthon et al., 2017). The evidence of such a phenomenon is quite recent as conventional capacitive thermo-hygrometers deployed on weather stations fail to report supersaturation because the excess of water vapour with respect to saturation condenses on the sampling device and the sensor (Genthon et al., 2017). The recent development and deployment of advanced thermo-hygrometers able to sample supersaturations on a 45-m mast (Genthon et al., 2022) at the French-Italian Concordia station on the Dome C, East Antarctic Plateau, paves the way for an examination of the humidity evolution during ice fog formation and

could give insights into the microphysical processes - including the nucleation and growth of ice crystals - that are potentially involved.

The objective of the present paper is to study the development of ice fog that do not have a liquid origin and do not correspond to maritime advections but that form locally at $T < 235$ K over the East Antarctic Plateau. Two case studies are analysed in details through an in depth examination of meteorological data at Dome C, a site particularly known for its very stable boundary layers and extreme temperature inversions (Vignon et al., 2017).

2 Data and methods

The French-Italian Concordia station is located on the Dome C, high Antarctic Plateau (75°06' S, 123°20' E, 3233 m a.s.l, Local Time LT = UTC+8 h). The landscape is a homogeneous and flat snow desert where the monthly mean 2 m temperatures ranges from about 246 K in austral summer to about 208 K in the polar night in winter (Genthon et al., 2021). During austral summer, the atmospheric boundary layer experiences a marked diurnal cycle with an alternation of diurnal shallow convection - when the sun is high above the horizon - and nocturnal stable stratification. Conversely during winter, the boundary-layer is almost always stably - even very stably - stratified (Genthon et al., 2013). The absence of terrain slope precludes the local generation of katabatic winds. The near-surface wind is mostly south-southwesterly and the annual 3 m mean speed is 4.5 m s^{-1} (Argentini et al., 2014). Occurrences of significant wind-transported snow events are seldom (Libois et al., 2014). The sets of observational data collected at the station and used in this study are described in the following sub-sections.

2.1 Wind, temperature and radiative flux measurements

Wind and temperature measurements are performed at six levels on a 45-m mast located 1-km upwind of Concordia station. Temperature is measured using mechanically-ventilated Vaisala HMP-155 thermo-hygrometers and wind speed and direction are obtained with R. M. Young 05103 aerovanes. 30-min average data have been used in this paper. Details on data acquisition and processing are given in (Genthon et al., 2021). The downward long-wave and short-wave radiative fluxes are measured at the Dome C Baseline Surface Radiation Network (BSRN) station using two Kipp and Zonen CM22 secondary standard pyranometers and two Kipp and Zonen CG4 pyrgeometers (Lanconelli et al., 2011; Driemel et al., 2018).

2.2 Humidity measurements

The near-surface atmosphere over the Antarctic Plateau is frequently supersaturated with respect to ice, which prevents from correctly measuring humidity with conventional capacitive hygrometers since the excess of moisture with respect to saturation condenses once the air gets in contact with the sampling device or the sensor (Genthon et al., 2017). The humidity data used in this study were obtained with advanced HMP-155 thermohygrometers deployed at three levels on the 45-m mast (Genthon et al., 2022). In a nutshell, the innovative technology behind these adapted HMP-155 consists of heating the air aspirated in the intake such that the sensor always samples an under-saturated air. A separate thermometer measures the ambient air temperature in order to retrieve the relative humidity with respect to liquid phase (RHl) of the ambient air. The calculation is

perfomed using the recent formula for the saturation vapor pressure wrt liquid phase obtained in Nachbar et al. (2019). Note that similar temperature conversions are applied for airborne hygrometers for which the sensor temperature differs from that of the ambient air (Neis et al., 2015). Relative humidity with respect to ice (RHi) is then calculated using the saturation vapor pressure wrt ice phase formula from Murphy and Koop (2005).

These innovative and low-cost hygrometers compare very satisfactorily with 'reference' frost point hygrometers (Genthon et al., 2017) but unlike the latter, they are further capable to operate in extremely cold conditions, even at temperatures < 220 K, which frequently occur at Dome C. Estimations of RHl and RHi uncertainties associated with the humidity and temperature measurements are provided in Appendix A and further details on the measurement system and the humidity data are provided in Genthon et al. (2017, 2022).

Regarding the specific humidity measurements in cloudy conditions, it is also worth mentioning that the intakes of the hygrometers are oriented downward such that sedimenting ice crystals cannot directly fall into the measurement system. Nevertheless, if the instrument is embedded in a foggy air, some ice particles may enter from below due to turbulent eddies and the mechanical aspiration. We have therefore analytically estimated the effect of sublimation of thin-fog ice particles – with a typical size of about 10 μm (Santachiara et al., 2016) and a typical number concentration of 0.5 cm^{-3} (Baumgartner et al., 2022) - on the RHl measurements (not shown). The obtained RHl change values are of the order of a few percents at most depending on the ice crystal shape assumption, on the ambient temperature and relative humidity values, and on the fraction of particles that sublimate. In any case, the obtained values are lower than the instrumental uncertainties calculated in Appendix A. The sublimation effects can therefore be deemed second order with respect to the intrinsic temperature and RHl measurement uncertainties.

To detect the possible occurrence of homogeneous freezing of solution aerosols, we will compare our RHi measurements with the so-called Koop et al. (2000)'s *threshold*. In the approach of Koop et al. (2000), solution particles spontaneously freeze when RHi exceeds a threshold value that primarily depends on temperature. As a first approximation, we calculate the RHi threshold value (RHi_T, in %) using the analytical fit of Koop et al. (2000)'s experimental results derived in Ren and Mackenzie (2005):

$$RHi_T = (2.349 - T/259) \cdot 100 \tag{1}$$

where T is the temperature in Kelvin. This fit has been performed for solution particles in equilibrium with the ambient vapor that have a typical radius of 0.25 μm and that can freeze homogeneously within 1 min (see also Kärcher and Burkhardt, 2008). The exact value of the threshold also depends on the size of the particle as well as on the composition thereof and on the formulation and uncertainties of water activities and saturation vapor pressure. Individually, those effects make RHi$_T$ vary by about 1 to 5 % (see Baumgartner et al., 2022). An envelop of 5 % has therefore been added around the Koop's curve in our graphs. This envelop is only intended as a rough indicator of the uncertainty and to guide the eye.

2.3 Radiosounding data

Vaisala RS92 radiosondes are released every day at 2000 LT (1200 UTC) from the Routine Meteorological Observation program (http://www.climantartide.it/) and processed with the standard Vaisala evaluation routines. Note that the actual launching time is around 1900 such that the sonde reaches the tropopause at 2000 LT. No temperature and humidity correction for time-lag errors has been applied since our analysis mostly focuses on the near-surface atmosphere (where the time-lag effect is negligible, Tomasi et al., 2012). Moreover, the relative humidity bias for standard RS92 measurements is relatively small: lower than 5% in magnitude across the whole troposphere at Dome C according to Tomasi et al., 2012.

2.4 Lidar measurements

A tropospheric depolarization aerosol lidar (532 nm) has been operating at Dome C since 2008 (http://lidarmax.altervista.org/englidar/Antarctic%20LIDAR.php). The lidar provides 5 min tropospheric profiles of aerosols and clouds continuously, from 20 to 7000 m a.g.l., with a 7.5 m vertical resolution. Further technical details are given in (Palchetti et al., 2015; Ricaud et al., 2020). Note that only the lidar backscattering signal is shown in this study but the investigation of the depolarisation ratio (not shown) reveals high values (>10%) for the two fog events analysed in this study. This suggests that the ice fogs do not contain supercooled liquid droplets, which is consistent with the temperature (<235 K) at which they are observed. To support the interpretation of lidar data, time-lapse webcam videos of local sky conditions are also collected.

2.5 Back-trajectory analysis

To ensure that the studied fog events correspond to local cloud formation over the Antarctic Plateau and are not associated with maritime air intrusions, we estimate air parcel Lagrangian back trajectories using the HYSPLIT modeling system (https://www.ready.noaa.gov) applied to the Global Data Assimilation System analysis of the National Center for Environmental Prediction with a horizontal grid of $0.5^o \times 0.5^o$ and a hourly temporal resolution. We calculate 2-day trajectories starting - backward in time - at the 4 closest grid points to Dome C and at two different heights near the surface: 50 m a.g.l. and 100 m a.g.l. We will see hereafter that the maximum ice fog depth during the events of interest is about 200 m. Assuming a fall velocity of $\approx 1 \text{ cm s}^{-1}$, ice crystals forming at the top of the fog layer reach the ground in less than 6 h. Therefore, a 2-day trajectory duration is sufficient to track the trajectories of the air masses probed above Dome C.

3 Results and discussion

3.1 Event 1: 7-9 March 2018

3.1.1 Overview

The first ice fog event we focus on occurred between the 7 and 9 March 2018. A picture showing the landscape of Dome C in the shallow and thin fog during sunset, 8 March 2018 is shown in Fig. 1. Fig. 2 shows a time-height plot of the lidar
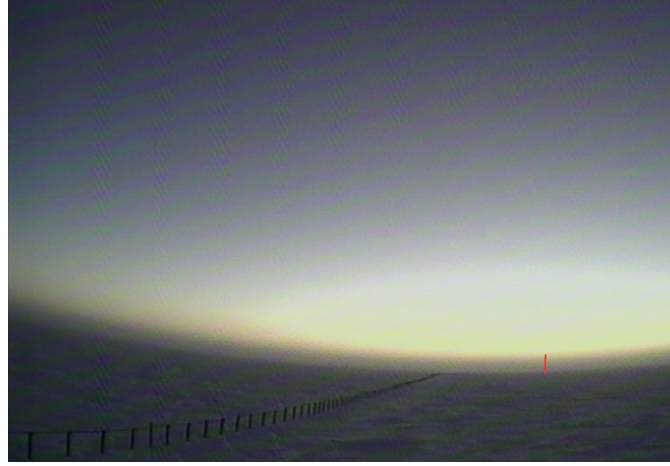
Figure 1. Webcam image of the ice fog at 12 UTC (20 LT), 8 March 2018 at Dome C. The shallow and thin fog layer manifests as a thin dark band above the horizon (delimited with a red line).
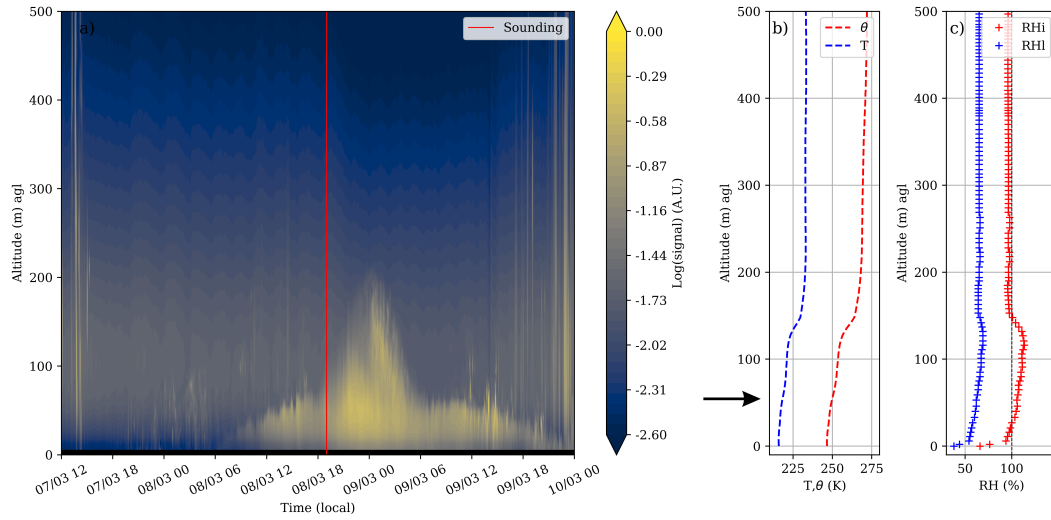

Figure 2. Panel a: Time-height plot of the lidar backscattering signal intensity during the first fog event between 12 LT, 8 March to 00 LT, 10 March 2018. The red line indicates the radiosonde launching time. Panel b shows the vertical profile of temperature (blue) and potential temperature (calculated with a reference pressure of 10^5 Pa, red) from the radiosounding. The black arrow indicates the top of the boundary layer. Panel c shows the vertical profile of relative humidity with respect to ice (RHi, red) and with respect to liquid water (RHl, blue) from the same radiosounding.
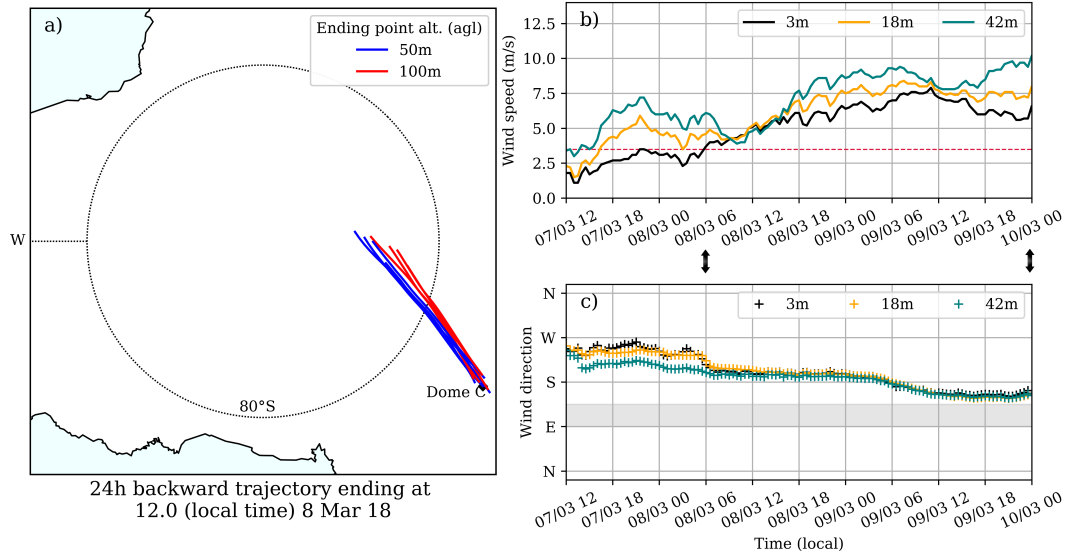
Figure 3. Panel a: 2-day back-trajectories ending at 50 m a.g.l. (blue) and 100 m a.g.l. (red) at the closest-to-Dome C four grid points. Panels b and c show the time series of the wind speed and origin at three levels on the mast. The dashed red line in panel b indicates the 3-m wind speed threshold value for snowdrift triggering (see details in the main text). The grey band in panel c delimits the wind direction range in which the flow can be possibly affected by station exhausts. Black arrows indicate the times at which the fog visually appears and disappears near the surface in the lidar measurements.

backscattering signal during the event. A clear shallow fog layer starts to develop from about 0600 LT, 8 March and grows from the ground until it reaches a maximum height of 200 m at 0100 LT, 9 March. Its depth then sharply decreases until 0600 LT and the decay continues until dissipation at 00 LT, 10 March.

The radiosounding reveals a layer supersaturated with respect to ice from 40 m to 150 m a.g.l. The maximum RHi value of 113 % is reached at 130 m a.g.l which roughly corresponds to the upper limit of the fog layer and of the boundary-layer top inversion at this time. The temperature between the ground and 120 m ranges between 216 K at the bottom and 230 K at the top (Fig. 2b) which confirms that the fog develops in cirrus-like temperature conditions.

The 3-m wind slightly veers from a south-westerly to a south-easterly direction and its magnitude increases throughout the event from 2 to 7.5 m s^{-1}. Libois et al. (2014) identify drifting snow events at Dome C when the 10-m wind speed exceeds 7 m s^{-1}. Assuming a logarithmic wind speed profile between the surface and 10-m and an aerodynamic roughness length value of 1 mm (Vignon et al., 2016), this corresponds to a 3-m wind speed threshold value of 3.5 m s^{-1}. Note that at 2200 LT, 7 March and after 0600 LT, 8 March, the 3-m wind speed exceeds the threshold and some snow drift is therefore possible during those periods.

As the air is coming from the southern sector, we do not expect this fog to be associated with an oceanic intrusion. It rather corresponds to a cloud that forms locally or slightly upstream over the Antarctic Plateau. This is confirmed by the analysis
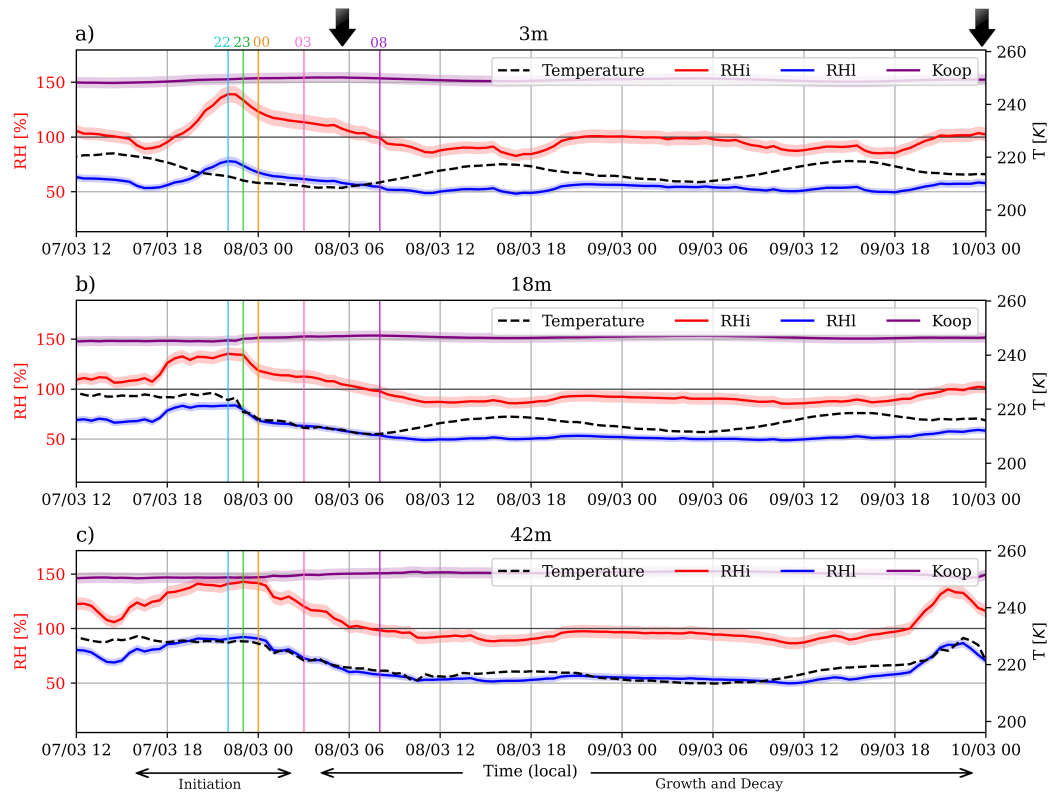
Figure 4. Time series of the temperature (dashed black line) and relative humidity with respect to ice (RHi, solid red line) and liquid water (RHl, solid blue line) at 3 m a.g.l (a), 18 m a.g.l. (b) and 42 m a.g.l. (c). The red and blue shading show the RH uncertainty ranges as estimated in Appendix A. The purple line shows the Koop et al. (2000)'s homogeneous freezing RHi threshold value. The 100 % RH value is highlighted with a solid black line. Vertical colored bars indicate the times at which vertical profiles are analysed in Fig. 5. Black arrows indicate the times at which the fog visually appears and disappears near the surface in the lidar measurements.

of air mass back-trajectories arriving at 50 and 100 m a.g.l. shown in Fig.3a. As the temperature along the trajectories never
165   exceeds 235 K (not shown), an advection of supercooled liquid droplets towards Dome C is unlikely which confirms that the
fog does not have a liquid origin

    Temperature measurements on the mast remain below 235 K throughout the event and one can notice a weak diurnal cycle
at 3-m that is almost totally damped at 42-m (Fig. 4). A close investigation of the vertical profile of the potential temperature -
very close to absolute temperature over the mast depth - reveals that the boundary layer transits between a weakly convective
170   state during daytime to a stable state during nighttime. The fog does not have a clear radiative signature at the surface even
though a slight decrease in downward longwave radiation is noticeable during the evening of 7 March (Fig B2a), which concurs
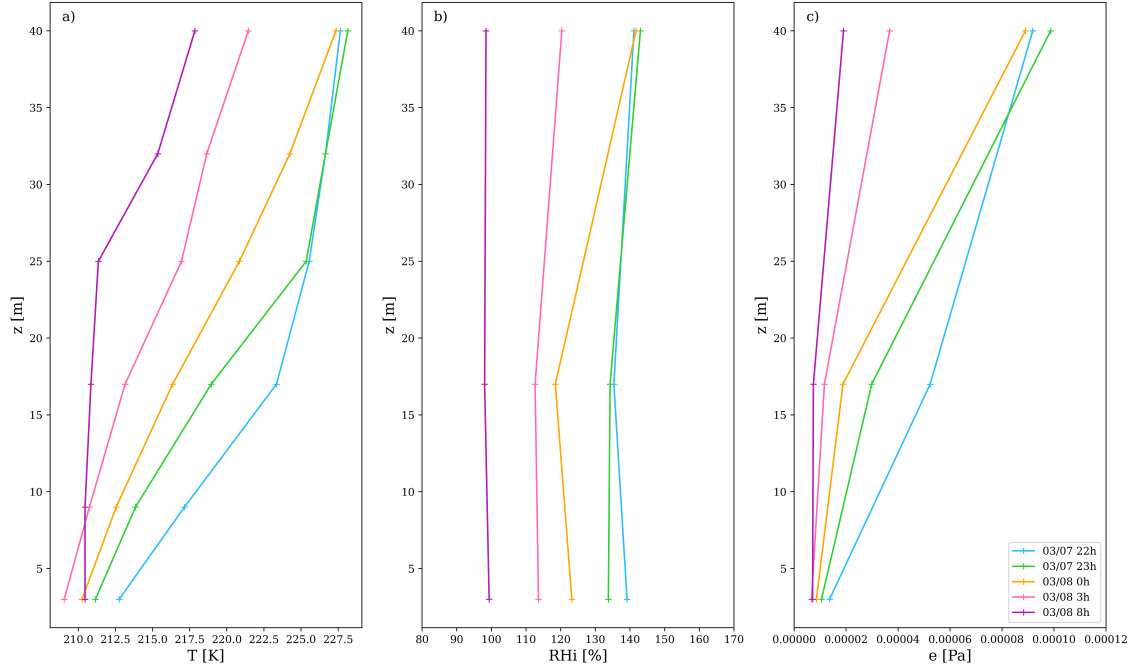with the overall decrease in air temperature (Fig 4).

Figure 5. Vertical profiles of temperature (a), relative humidity with respect to ice (b) and vapor partial pressure (c) at different times during the fog development phase.

3.1.2 Fog initiation: 1500 LT, 7 March to 0300 LT, 8 March

We now focus on the initiation period from 1500 LT, 7 March to 0300 LT, 8 March. At the 42-m level, RHi first exhibits an

175 increase from 106 % to 143 % which coincides with an increase in vapor partial pressure. At the 3-m level, a later but sharper increase in RHi up to 139 % at 2200 LT, 7 March is noticeable and unlike at 42-m and 18-m, this increase is partly explained by a decrease in temperature during the day-night transition. The maximum RHi reached at the three levels ranges between 139 and 143 %. RHl remains lower than 78 % at 3-m but it exceeds 90 % at 42 m at 2300 LT, 7 March.

RHi then gradually decreases and reaches 100 % at the three levels at 0800 LT, 8 March (Fig. 4). The decrease starts at 2230

180 LT, 7 March at the 3-m level, a half-hour later at 18-m and 2 hours later at 42-m.

Given the maximum RHl and RHi values attained, the aerosol deliquescence and solution droplet freezing at 3-m a.g.l. are not very likely but their occurrence cannot be completely excluded since Baumgartner et al. (2022) show that homogeneous freezing can start at RHi values slightly lower than the Koop et al. (2000)'s threshold. As the station exhausts do not affect our measurements (see grey shading in Fig. 3c), the decrease in 3-m relative humidity from 2200 LT can therefore be explained

185 either by *i)* ice nucleation and vapour deposition onto newly formed ice crystals and/or by *ii)* a net downward turbulent moisture flux towards the ground surface as the vertical gradient of vapor partial pressure is positive (see Fig. 5c) and/or by *iii)* the vapour deposition of drifting ice crystals in the surface layer although the erosion threshold is barely attained.

9

At 18-m, the decrease in RHi from 2200 LT is co-incidental with a sharp decrease in vapour partial pressure as well as a decrease in gradient of vapour partial pressure (Fig. 5c) between 3 and 18-m. The 18-m drying from 2200 LT is therefore due to the turbulent mixing near the suface with a net flux of a moisture oriented downward.

At 42-m, a similar decrease in relative humidity and temperature is observed but the particularity of this level, and probably that of the overlying air layers is that RHi gets very close to the Koop et al. (2000)'s RHi threshold for homogeneous freezing of solution droplets in the middle of the night (see time series in Fig. 4c and how the system evolves in a RH-temperature space in B1). The difference between the RHi value and the homogeneous freezing threshold is even smaller than the measurements uncertainty (red shading in Fig. 4c). We can therefore assume that the ice fog forms a few tens of meters above the ground surface through homogeneous nucleation and the subsequent decrease in RHi at 42-m is therefore partly explained by the vapour deposition onto newly formed ice crystals. A few patches of ice fogs are noticeable during the night between the 7 and 8 March (Fig. 2a).

3.1.3 Growth and decay: 0300 LT, 8 March to 2300 LT, 9 March

From 0300 to 0800 LT, 8 March, the temperature vertical profile shows a clear night-day transition i.e. a transition from an 'exponential' shape characteristic of very stable boundary layers to a convective profile with a well-mixed layer capped by a shallow temperature inversion whose height further increases during the day (Fig. 5a). A close inspection of the vertical profile of specific humidity between 3-m and the surface at 0800 LT (not shown) - assuming that the specific humidity at the snow surface equals the saturation specific humidity at the surface temperature - reveals that the vertical gradient of specific humidity and subsequently the surface flux of water vapour reverses sign and become oriented upward. The supply of water vapour from the snow surface - and possibly of drifting ice crystals since the surface wind speed exceeds the erosion threshold (Fig. 3b) - can therefore deposit onto the ice crystal embryos nucleated in the early morning and make them grow and become visible in the lidar signal.

Fig. 2a shows that the depth of the fog layer gradually increases from 0600 LT, 8 March up to about 80 m at 1800 LT, 8 March, as the daytime convective boundary layer deepens in $\approx \sqrt{t}$ (Stull, 1990). The growth of the fog is possible in the higher part of the boundary layer as its top is supersaturated wrt ice (Fig 2c). Ice crystals can hence grow by vapour deposition and sediment down to the near-surface layers where they probably partly sublimate (Fig. 2 and 4). Concurring with Genthon et al. (2022) (see their Fig. 8), the near-surface air becomes subsaturated wrt ice particularly during daytime when the near-surface air warms by convective mixing. As night falls around 19 LT, 8 March, one can then note a sharper deepening of the fog up to 200 m. The mechanisms responsible for this sudden growth cannot be directly identified from our measurements but one can nonetheless make some assumptions. As the wind speed increases in the late afternoon (Fig. 3b), one could expect an enhanced vertical mixing of ice particle but a close examination of the wind speed profile from the radiosonde reveals a weak local wind shear at the top of the boundary-layer. Nonetheless, in the late afternoon, the decrease in the shallow convection intensity leads to a decrease in the capping temperature inversion strength (Ricaud et al., 2012). The weak vertical gradient of temperature at the top of the evening convective boundary layer is visible in Fig. 2b (see black arrow) whereas a second higher and stronger temperature inversion is visible at the top of the fog layer and probably induced by the cloud-top radiative cooling.
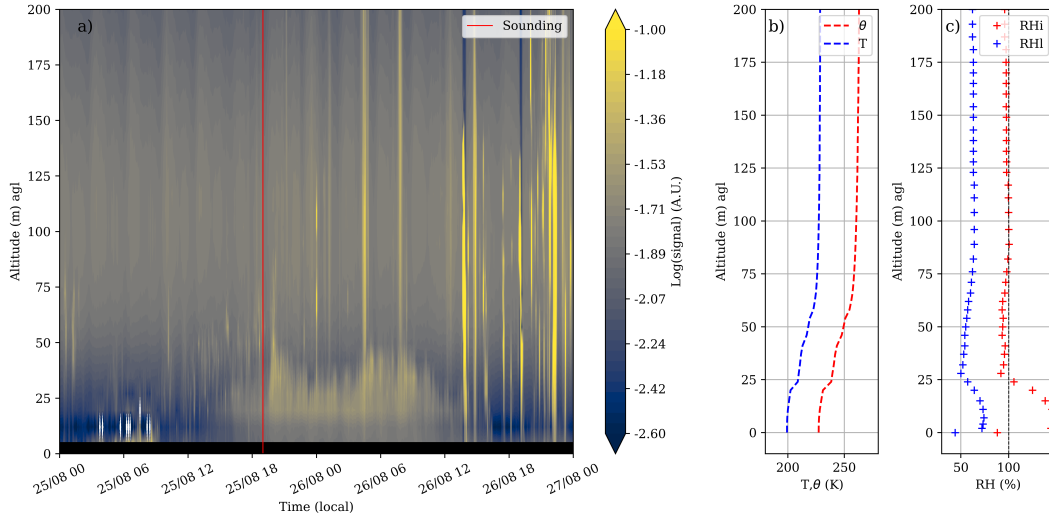
Figure 6. Same as Fig. 2 but for Event 2.

Izett and van de Wiel (2020) show that the growth of a radiative liquid fog layer can suddenly accelerate when the vertical gradient of temperature decreases (i.e. when the vertical gradient of saturation specific humidity decreases, see their Eq. 7). If we assume a homogeneous freezing process, the ice nucleation occurs at the Koop et al. (2000)'s threshold, that is, according to an increasing function of temperature. Subsequently, we can reasonably think that the conceptual model of Izett and van de Wiel (2020) is qualitatively valid for our ice fogs. We can therefore assume that during the evening of the 8 March, the ice fog grows radiatively and the depth of the layer sharply increases due to the decrease in the temperature vertical gradient. It is worth noting that the growth rate of the fog layer (about 120 m in 7 h from visual inspection of Fig. 2a, that is $\approx 17 \text{ m h}^{-1}$) is quite similar to the growth rate of the radiative liquid fog portrayed in Izett and van de Wiel (2020) during the acceleration phase.

The fog grows until it reaches the top of the atmospheric layer supersaturated with respect to ice. From 1800 LT, 8 March to 0600 LT, 9 March, the RHi at the three levels is ≤ 100 % (Fig. 4) - in agreement with the radiosounding shown in Fig. 2c - while the lidar detects ice condensates from the surface up to 200 m a.g.l. The top-height of the fog layer then drops down to about 50 m at 0700 LT, 9 March and then slightly increases back at a time which correspond to the deepening of the shallow-convective diurnal boundary layer. The fog layer then becomes shallower and shallower from 1500 LT, 9 March as the turbulent mixing in the boundary layer weakens. The fog vanishes during the evening of the 9 March and RHi and temperature at 42-m increase up to their values before fog formation.
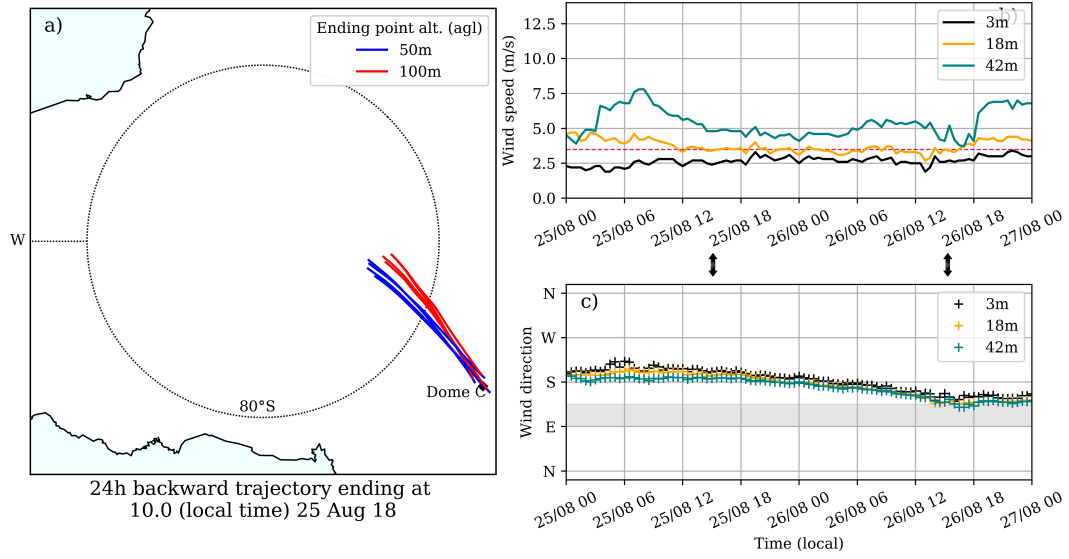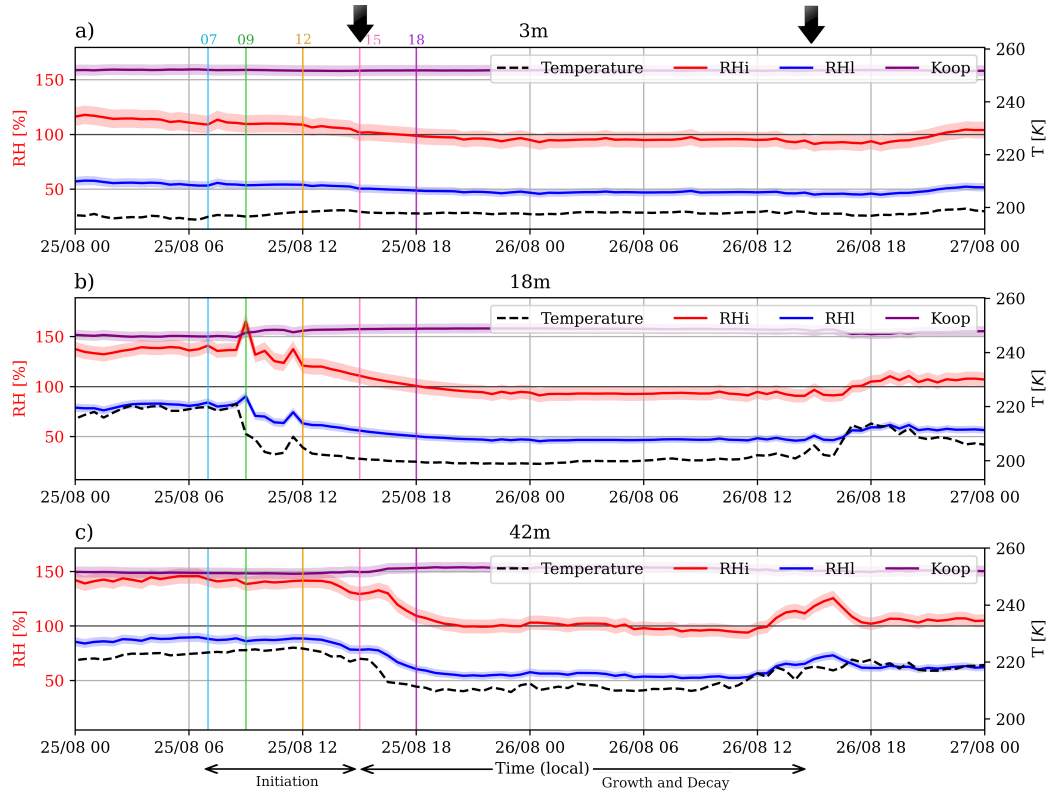
11

Figure 7. Same as Fig. 3 but for Event 2.

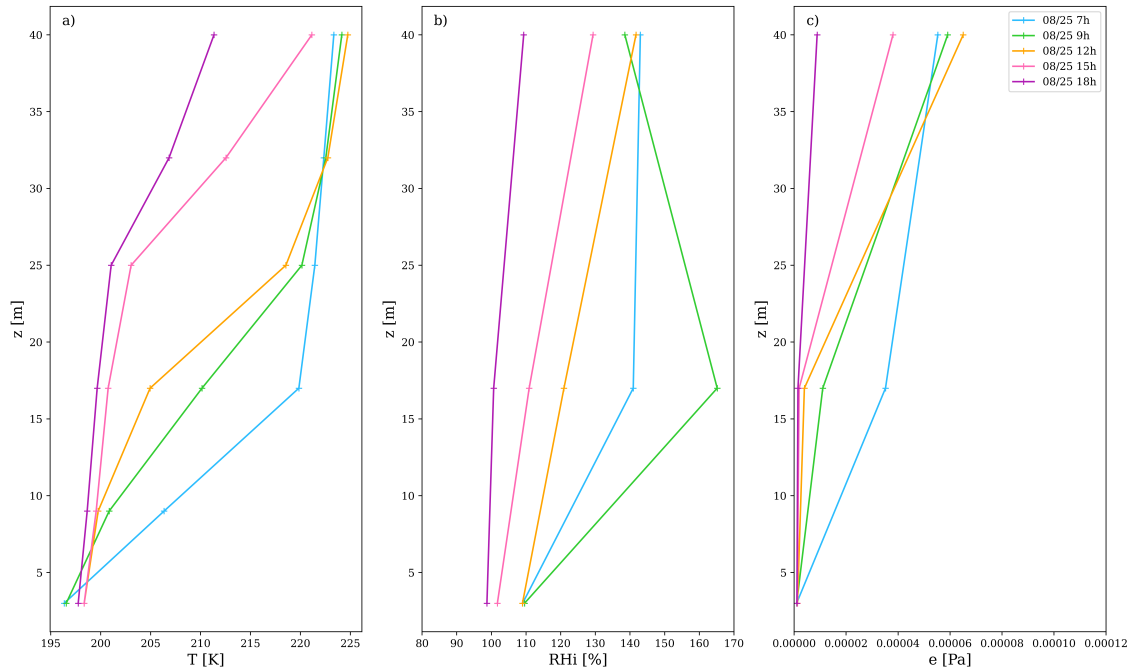**Figure 8.** Same as Fig. 4 but for Event 2.

Figure 9. Same as Fig. 5 but for Event 2.

3.2 Event 2: 25-27 August 2018

3.2.1 Overview

The second case study occurred between the 25 and 27 August 2018. No picture is available since the sun is almost always below the horizon during this period of the year. At 1500 LT, 25 August a very shallow - about 20 m deep - ice fog starts to be visible in the lidar profiles (Fig. 6a). Its depth then oscillates between 25 and 50 m a.g.l. and the fog vanishes at around 1400 LT, 26 August. This event is particularly interesting since its vertical extent is almost the same as the one of the meteorological mast. Note that highly reflective bands are observed during the 26 August and most of them correspond to diamond dust precipitation 'peaks' falling from the mid-troposphere. The radiosounding reveals a supersaturated layer with respect to ice below 30 m a.g.l. with a maximum RHi value of 147 %. The relative humidity with respect to liquid water also exceeds 75% near the surface (Fig. 6c).

Fig. 7b shows that the 3-m wind speed remains below 4m s^{-1} throughout the event and never exceeds the threshold value to trigger drifting snow. Its direction slightly changes from south-westerly to a south-easterly suggesting that the air parcels reaching Dome C come from the high Antarctic Plateau (Fig. 7b) and that our measurements are not affected by station exhausts except during the very end of the event (see grey shading in Fig. 7c). The back-trajectories shown in Fig. 7a confirm the continental origin of the flow and as the temperature measured at the station is much lower than 235 K, a liquid-origin of

13

the fog can be ruled out. The time-series of observational data along the mast reveal a near-constant 3-m temperature of about 200 K during the event and confirm the absence of diurnal cycle during this period of the year.

3.2.2 Fog initiation: 0600 to 1500 LT, 25 August

A significant drop in temperature at 0900 LT is observed at 18-m. This cooling is due to an abrupt transition between a very stable to a weakly stable dynamical regime of the boundary-layer (van de Wiel et al., 2017; Baas et al., 2019; van der Linden et al., 2019) driven by an increase in the synoptic wind speed (note that the wind at 42-m, i.e. at the top or above the shallow boundary layer, is a reasonable proxy of the synoptic wind, see Fig. 8c). Subsequently the temperature profile evolves from a typical 'exponential' shape to a concave shape (Vignon et al., 2017) owing to a more vigorous turbulent transport of heat towards the surface (Fig. 9). At 18-m the cooling rate is particularly intense and equals 5 K h^{-1} between 0800 and 1100 LT, 25 August. As an analogy with typical air parcel cooling within updraft in the mid- and high-troposphere, such a cooling rate roughly corresponds to an adiabatic air ascent of 0.10 m s^{-1}.

At 42-m, RHi approaches the Koop et al. (2000)'s threshold between 0400 and 0500 LT 25 August and some preliminary crystal nucleation can already occur at this time. However at 0900 LT, 25 August RHi at 18-m suddenly increases as temperature drops and clearly exceeds the Koop et al. (2000)'s homogeneous freezing threshold. RHl exceeds 90% at the same time (see Fig. 8b and B1). The relative humidity does not substantially change at the two other levels at this time, leading to a well marked maximum in the vertical profile (Fig. 9b). It is worth mentioning that Genthon et al. (2022) show that the climatological RHi along the mast also exhibits a clear maximum at 18-m due to non-linear dependence of relative humidity on temperature and atmospheric water content. Therefore, the initiation of the second fog event seems mainly due to a homogeneous freezing process starting between 3 and 42 m a.g.l around 0900, 25 August. The density and size of ice crystals become sufficiently large for being well visible in the lidar signal a few hours later. From 1000 LT, 25 August, RHi at 18-m starts a pronounced decrease due to the vapour deposition onto newly-formed crystals and to a downward turbulent flux of water vapour as the vertical gradient of vapour partial pressure between 3 and 18 m is positive (Fig. 9c).

3.2.3 Growth and decay: 1500 LT, 25 August to 1500 LT, 26 August

The decrease in RHi at 42-m occurs at 1500 LT and it coincides with a decrease in temperature associated with the deepening of the weakly stable boundary layer (Fig. 8c and 9a). The decrease in the 42-m RHi also concurs with the increase in fog layer depth visible in the lidar data between 1500 and 1800 LT, 25 August (Fig. 6a) and can therefore be attributed to the deposition of water vapor onto ice crystals. The saturation is reached at 1900 LT, 25 August.

From the evening of the 25 August, RHi remains close but slightly below saturation at 3 and 18 m probably owing to a net flux of vapor towards the surface in the very shallow boundary layer. Ice crystals at these two heights can therefore not grow very close to the surface but their detection at 18 m by the lidar may be rather explained by some sedimentation from higher layers.

285   At 1200 LT, 26 August, the fog starts to dissipate from the top and the air at 42-m becomes supersaturated wrt ice (Fig. 8c). A few hours later a decrease in RHi back to saturation occurs probably due to vapor deposition onto the diamond dust precipitation streaks that suddenly fall down from the low- and mid- troposphere (Fig. 6a).

4   Summary and conclusions

Temperature and humidity measurements from advanced thermohygrometers along a 45-m mast are combined with lidar and
290 radiosonde observations and air-parcel back-trajectories to study the development of two fog events at cirrus temperatures in the near-surface atmosphere of Dome C, high Antarctic Plateau. For both case studies, fog forms locally and does not correspond to warm maritime intrusions. Lidar observations evidenced shallow fogs and the innovative moisture measurements along the tower allowed us to explain the mechanisms responsible for their formation.

     Fig 10 summarises the development of the fogs with two schematics. The values of supersaturation that are attained and the
295 very low temperatures that prevent the pre-existence of supercooled liquid droplets suggest that the two fogs are initiated by the homogeneous freezing of solution aerosols in the stably stratified boundary layer. This study presents the first observational evidences that this process can be responsible for the formation of an ice fog. The highest supersaturations occur at a height where the air cools down by turbulent mixing and radiation and where the downward flux of water vapour is sufficiently weak. The evolution of the fog is thereby tightly related with the turbulent dynamics of the boundary-layer which experiences a weak
300 diurnal cycle in the first study case and a dynamical transition between a very stable and a weakly stable state in the second case.

     Regarding the potential similarity between Antarctic ice fogs and cirrus clouds, this study suggests that the homogeneous freezing of solution particles, i.e. a common path to cirrus cloud formation, can be studied in natural conditions near the ground surface of the Antarctic Plateau. More generally, it emphasises that Dome C is a relevant place to carry out observational studies
305 of microphysical processes in ice clouds. Furthermore, the analysis of humidity measurements during the growing phase of fog gives access to the time-scale at which the vapour is depleted, even though it is particularly delicate to disentangle the dynamical - i.e. turbulent mixing - from the microphysical - i.e. deposition onto ice crystals - causes. The development of the fogs is indeed tightly coupled with the dynamics of the boundary-layer. This is a non-negligible difference with cirrus clouds in which ice crystal properties strongly depend on the dynamics of gravity waves (e.g., Jensen et al., 2016) and local turbulent
310 eddies (e.g., Gultepe and Starr, 1995).

     While the available observations at Dome C make it possible to characterise the overall development of ice fogs, they do not give direct information about the type - homogeneous or heterogeneous - of the ice nucleation process and do not allow for a fine understanding of the interactions between cloud microphysics, radiation and turbulent dynamics. Collecting sedimenting ice crystals during ice fog events and establishing formvar replicas thereof in the manner of Santachiara et al. (2016) would
315 allow us to analyse the morphological structure of crystals and to perform chemical analyses of potentially remaining particles after sublimation. Running a large-eddy simulations with an advanced microphysical scheme for cold clouds and capable of simulating the boundary-layer at Dome C (Couvreux et al., 2020) would also help better understand the mechanisms driving
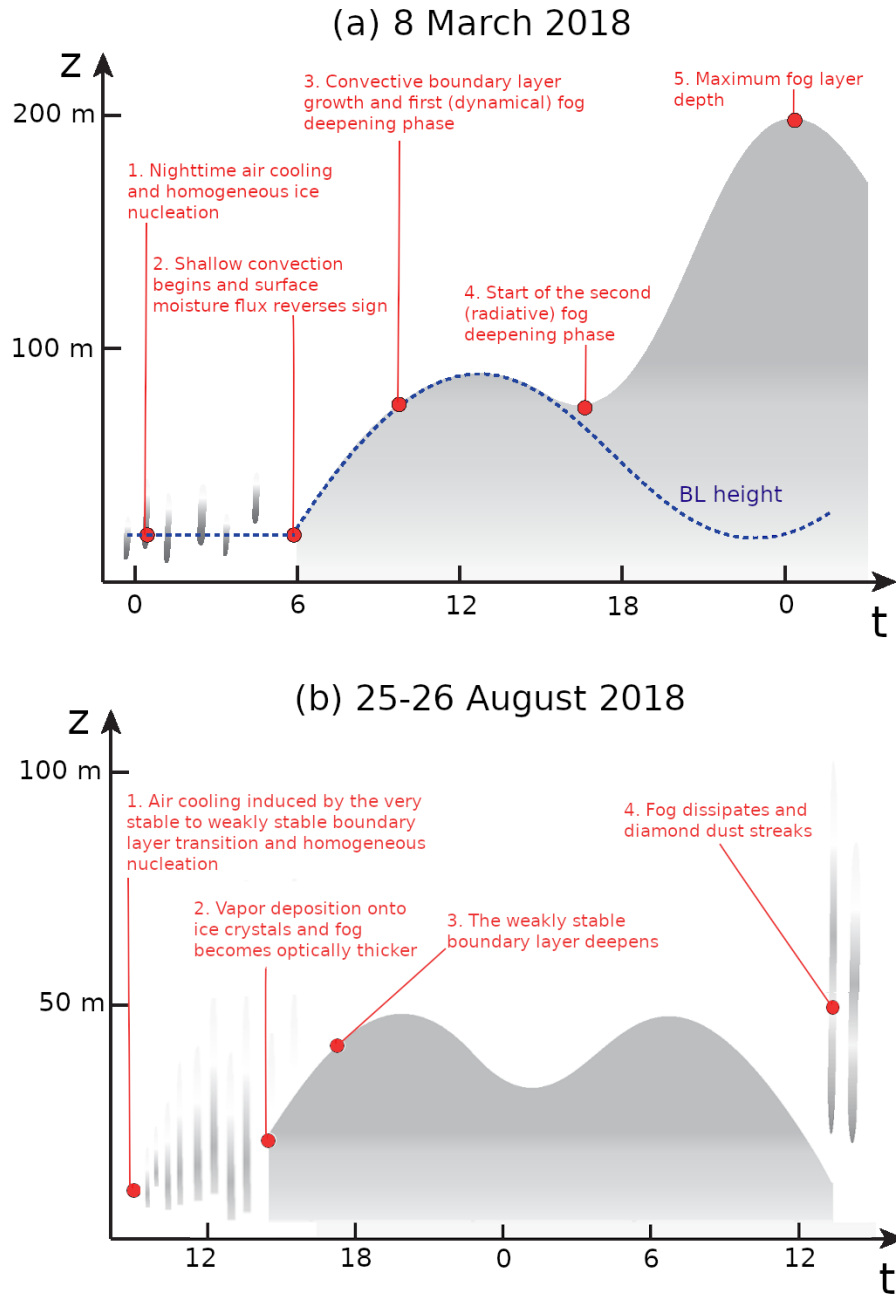
(a) 8 March 2018

3. Convective boundary layer growth and first (dynamical) fog deepening phase

5. Maximum fog layer depth

1. Nighttime air cooling and homogeneous ice nucleation

2. Shallow convection begins and surface moisture flux reverses sign

4. Start of the second (radiative) fog deepening phase

BL height

(b) 25-26 August 2018

1. Air cooling induced by the very stable to weakly stable boundary layer transition and homogeneous nucleation

4. Fog dissipates and diamond dust streaks

2. Vapor deposition onto ice crystals and fog becomes optically thicker

3. The weakly stable boundary layer deepens

Figure 10. Conceptual scheme of the formation and growth of the two ice fogs studied in the paper.

16

the growth and decay of the fogs. Furthermore, investigating the frequency of occurrence of very cold ice fogs at Dome C was beyond the scope of this study. This aspect would deserve further attention in the future to figure out their climatological impacts on the Antarctic Plateau.

320

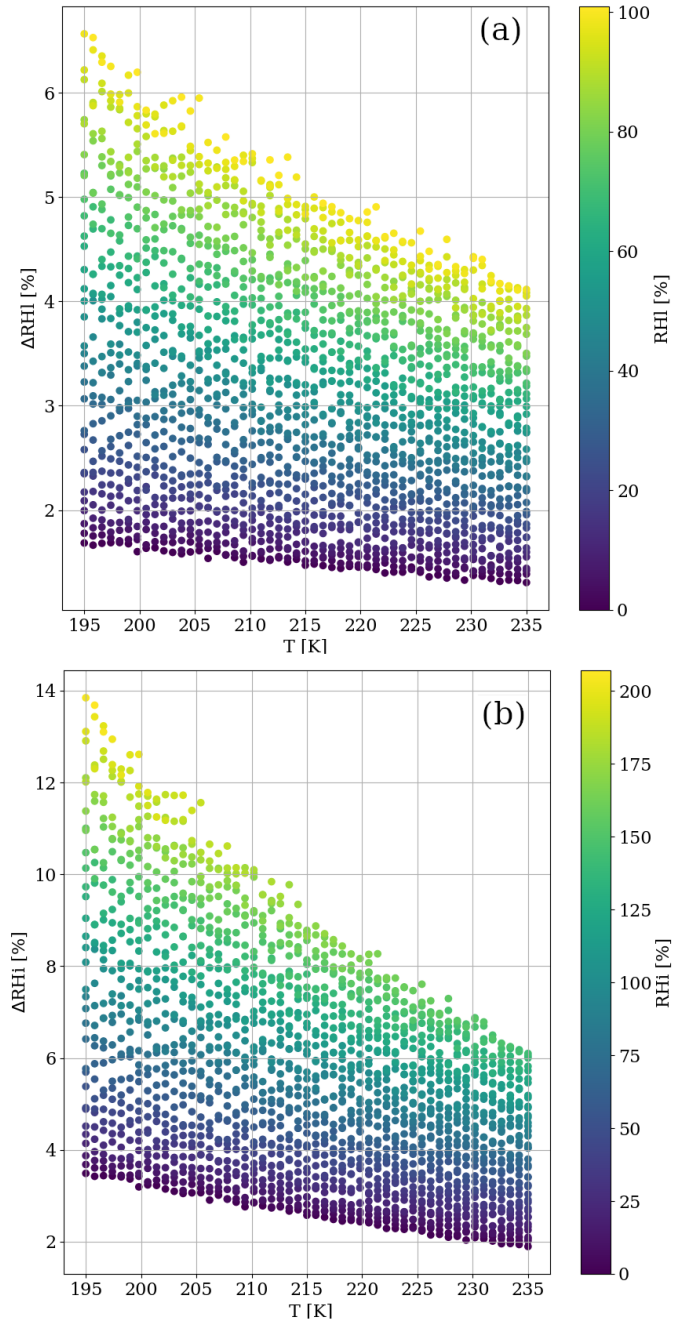# Appendix A: Uncertainties of relative humidity measurements

Figure A1. Panel a (resp. b): uncertainty in the RHl (resp. RHi) estimations as a function of temperature (x-axis) and RHl (resp. RHi) (color shading).

The estimation of RHl and RHi from the advanced thermo-hygrometers depends on (Genthon et al., 2017, 2022):

- the measurement of the relative humidity wrt liquid water in the heated inlet RHl_h by the HMP-155 probe;

- the measurement of the temperature of the heated inlet T_h by the HMP-155 (PT-100);

325   - the measurement of the ambient temperature T by the independent PT100 platinium resistance thermometer.

RHl and RHi are then calculated with the following expressions:

$$RHl = RHl_h \cdot e_{sl}(T_h)/e_{sl}(T) \tag{A1}$$

$$RHi = RHl \cdot e_{sl}(T)/e_{si}(T) \tag{A2}$$

with e_{sl} and e_{si} the saturation water pressure with respect to liquid and ice respectively and calculated with Murphy and
330   Koop (2005)'s formulae. According to the manufacturers, the accuracy of the relative humidity measurement below $-40°C$ is
$\pm 1.4 + 0.032$ of the reading in percentage and the accuracy of the temperature measurement is $0.226 - 0.0028 \cdot (T - 273.15)$.
To estimate the uncertainties in the RHl and RHi end-products, we perform a Monte Carlo test with a 1'000 uniform re-sample
of RHl_h, T_h and T in the interval [value - accuracy,value + accuracy]. The uncertainties ΔRHl and ΔRHi are evaluated as
one standard deviation of the obtained distributions for each bin of relative humidity and temperature. In the calculation, we
335   assume that the air reaching the hygrometer sensor in the heated inlet is ≈ 5 K warmer than the ambient air (mean over the
measurement period: 4.9 K, standard deviation: 0.7 K).

Panel a (resp. b) of Fig. A1 shows how the uncertainty in the RHl (resp. RHi) estimation depends on temperature. For each
temperature bin on the x-axis, the dependence is explored for different RHl (resp. RHi) values below liquid saturation (color
shading).

340   ΔRHl and ΔRHi can be expressed as continuous functions of relative humidity and temperature with a regression of the
form:

$$\Delta RHl, i = a_{0l,i} + a_{1l,i} RHl, i(a_{2l,i} T + a_{3l,i} T^2) \tag{A3}$$

with $a_{0l,i}$, $a_{1l,i}$, $a_{2l,i}$ and $a_{3l,i}$ the regression coefficients. The R^2 coefficients of the regression equal 0.990 and 0.993 for
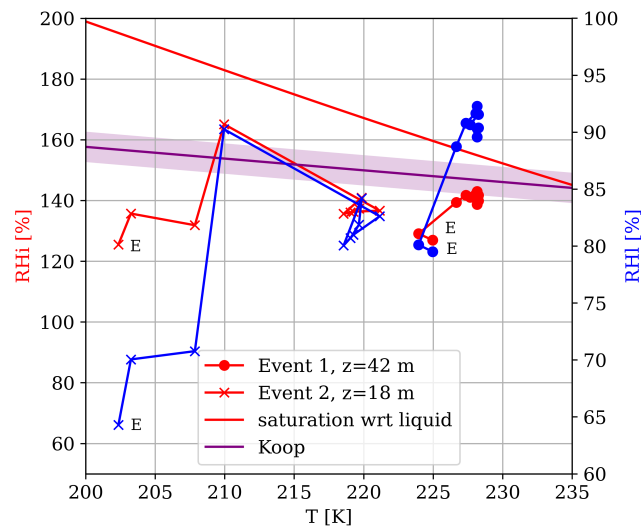ΔRHl and ΔRHi respectively.

Figure B1. RHi (red curves, left y-axis) and RHl (blue curve, right y-axis) evolution as a function of temperature at the level of nucleation during the initiation phase of the fog. Lines with circles refer to the first event (from 2100 LT, 7 March to 0200 LT, 8 March) while the lines with crosses refer to the second event (from 0600 to 1100 LT, 25 August). 'E' indicates the endpoint. The solid red line shows RHi value at liquid water saturation and the purple line the Koop et al. (2000)'s homogeneous freezing RHi threshold value
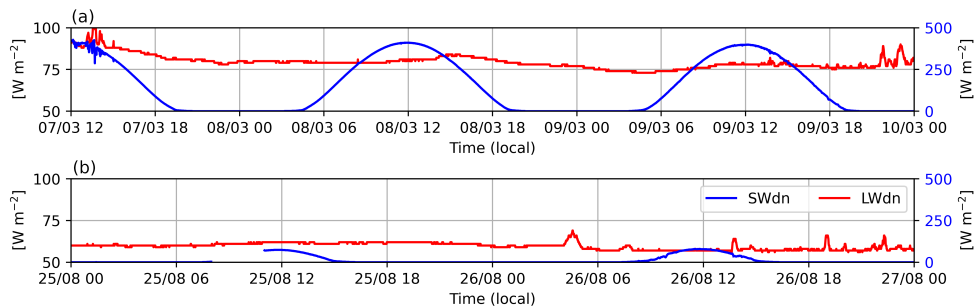
Figure B2. Time series of downward longwave (LWdn, red) and shortwave (SWdn, blue) radiative fluxes at the surface during the first (a) and second (b) case studies.

350   *Author contributions.* EV, LR and CG designed and conducted the study. LR and EV analysed the data and LR made the figures. MDG collected and processed the lidar data. CG collected and maintained the meteorological measurements on the mast at Dome C. AH, JBM and AB provided scientific expertise on cold microphysics and contributed to the results' interpretation. EV wrote the paper with contributions from all the authors.

Competing interests. The authors declare they have no competing interests.

References

Argentini, S., Pietroni, I., Mastrantonio, G., P., V. A., Dargaud, G., and Petenko, I.: Observations of near surface wind speed, temperature and radiative budget at Dome C, Antarctic Plateau during 2005, Antarct Sci, 26, doi:10.1017/S0954102013000382, 2014.

Baas, P., van de Wiel, B. J. H., van Meijgaard, E., Vignon, E., Genthon, C., van der Linden, S. J. A., and de Roode, S. R.: Transitions in the wintertime near-surface temperature inversion at Dome C, Antarctica, Quarterly Journal of the Royal Meteorological Society, 145, 930–946, https://doi.org/https://doi.org/10.1002/qj.3450, 2019.

Baumgartner, M., Rolf, C., Grooß, J.-U., Schneider, J., Schorr, T., Möhler, O., Spichtinger, P., and Krämer, M.: New investigations on homogeneous ice nucleation: the effects of water activity and water saturation formulations, Atmospheric Chemistry and Physics, 22, 65–91, https://doi.org/10.5194/acp-22-65-2022, 2022.

Belosi, F., Santachiara, G., and Prodi, F.: Ice-forming nuclei in Antarctica: New and past measurements, Atmospheric Research, 145-146, 105–111, https://doi.org/https://doi.org/10.1016/j.atmosres.2014.03.030, 2014.

Blanchet, J.-P. and Girard, E.: Water vapor-temperature feedback in the formation of continental Arctic air: its implication for climate, Science of The Total Environment, 160-161, 793–802, https://doi.org/https://doi.org/10.1016/0048-9697(95)04412-T, ecological Effects of Arctic Airborne Contaminants, 1995.

Couvreux, F., Bazile, E., Rodier, Q., Maronga, B., Matheou, G., Chinita, M. J., Edwards, J., van Stratum, B. J., van Heerwaarden, C. C., Huang, J., et al.: Intercomparison of large-eddy simulations of the Antarctic boundary layer for very stable stratification, Boundary-Layer Meteorology, 176, 369–400, https://doi.org/10.1007/s10546-020-00539-4, 2020.

Curry, J. A., Meyer, F. G., Radke, L. F., Brock, C. A., and Ebert, E. E.: Occurrence and characteristics of lower tropospheric ice crystals in the arctic, International Journal of Climatology, 10, 749–764, https://doi.org/https://doi.org/10.1002/joc.3370100708, 1990.

DeMott, P. J., Rogers, D. C., Kreidenweis, S. M., Chen, Y., Twohy, C. H., Baumgardner, D., Heymsfield, A. J., and Chan, K. R.: The role of heterogeneous freezing nucleation in upper tropospheric clouds: Inferences from SUCCESS, Geophysical Research Letters, 25, 1387–1390, https://doi.org/https://doi.org/10.1029/97GL03779, 1998.

Driemel, A., Augustine, J., Behrens, K., Colle, S., Cox, C., Cuevas-Agulló, E., Denn, F. M., Duprat, T., Fukuda, M., Grobe, H., Haeffelin, M., Hodges, G., Hyett, N., Ijima, O., Kallis, A., Knap, W., Kustov, V., Long, C. N., Longenecker, D., Lupi, A., Maturilli, M., Mimouni, M., Ntsangwane, L., Ogihara, H., Olano, X., Olefs, M., Omori, M., Passamani, L., Pereira, E. B., Schmithüsen, H., Schumacher, S., Sieger, R., Tamlyn, J., Vogt, R., Vuilleumier, L., Xia, X., Ohmura, A., and König-Langlo, G.: Baseline Surface Radiation Network (BSRN): structure and data description (1992–2017), Earth System Science Data, 10, 1491–1501, https://doi.org/10.5194/essd-10-1491-2018, 2018.

Driemel, A., Augustine, J., Behrens, K., Colle, S., Cox, C. J., Cuevas-Agulló, E., Denn, F. M., Duprat, T., Dutton, E. G., Fukuda, M., Grobe, H., Haeffelin, M., Hodges, G., Hyett, N., Ijima, O., Kallis, A., Knap, W., Kustov, V., Lanconelli, C., Long, C., Longenecker, D., Lupi, A., Maturilli, M., Mimouni, M., Ntsangwane, L., Ogihara, H., Olano, X., Olefs, M., Omori, M., Passamani, L., Pereira, E. B., Schmithüsen, H., Schumacher, S., Sieger, R., Tamlyn, J., Vogt, R., Vuilleumier, L., Xia, X., Ohmura, A., and König-Langlo, G.: Baseline surface radiation data (1992-2017), https://doi.org/10.1594/PANGAEA.880000, supplement to: Driemel, A et al. (2018): Baseline Surface Radiation Network (BSRN): structure and data description (1992-2017). Earth System Science Data, 10(3), 1491-1501, https://doi.org/10.5194/essd-2018-8, 2018.

Genthon, C., Six, D., Gallée, H., Grigioni, P., and Pellegrini, A.: Two years of atmospheric boundary layer observations on a 45-m tower at Dome C on the Antarctic Plateau, J Geophys Res Atmos, 118, doi:10.1002/jgrd.50128, 2013.

Genthon, C., Piard, L., Vignon, E., Madeleine, J.-B., Casado, M., and Gallée, H.: Atmospheric moisture supersaturation in the near-surface atmosphere at Dome C, Antarctic Plateau, Atmos Chem Phys, 17, 1–14, doi:10.5194/acp-17-1-2017, 2017.

Genthon, C., Veron, D., Vignon, E., Six, D., Dufresne, J.-L., Madeleine, J.-B., Sultan, E., and Forget, F.: 10 years of temperature and wind observation on a 45 m tower at Dome C, East Antarctic plateau, Earth System Science Data, 13, 5731–5746, https://doi.org/10.5194/essd-13-5731-2021, 2021.

Genthon, C., Veron, D., Vignon, E., Six, D., Dufresne, J. L., Madeleine, J.-B., Sultan, E., and Forget, F.: Ten years of wind speed observation on a 45-m tower at Dome C, East Antarctic plateau, https://doi.org/10.1594/PANGAEA.932513, 2021a.

Genthon, C., Veron, D., Vignon, E., Six, D., Dufresne, J. L., Madeleine, J.-B., Sultan, E., and Forget, F.: Ten years of wind speed observation on a 45-m tower at Dome C, East Antarctic plateau, https://doi.org/10.1594/PANGAEA.932513, 2021b.

Genthon, C., Veron, D., Vignon, E., Madeleine, J.-B., and Piard, L.: Water vapor observation in the lower atmospheric boundary layer at Dome C, East Antarctic plateau, https://doi.org/10.1594/PANGAEA.939425, 2022.

Genthon, C., Veron, D. E., Vignon, E., Madeleine, J.-B., and Piard, L.: Water vapor in cold and clean atmosphere: a 3-year data set in the boundary layer of Dome C, East Antarctic Plateau, Earth System Science Data Discussions, 2022, 1–25, https://doi.org/10.5194/essd-2021-412, 2022.

Girard, E. and Blanchet, J.-P.: Simulation of Arctic Diamond Dust, Ice Fog, and Thin Stratus Using an Explicit Aerosol–Cloud–Radiation Model, Journal of the Atmospheric Sciences, 58, 1199 – 1221, https://doi.org/10.1175/1520-0469(2001)058<1199:SOADDI>2.0.CO;2, 2001.

Gultepe, I. and Starr, D. O.: Dynamical Structure and Turbulence in Cirrus Clouds: Aircraft Observations during FIRE, Journal of Atmospheric Sciences, 52, 4159 – 4182, https://doi.org/10.1175/1520-0469(1995)052<4159:DSATIC>2.0.CO;2, 1995.

Gultepe, I., Zhou, B., Milbrandt, J., Bott, A., Li, Y., Heymsfield, A., Ferrier, B., Ware, R., Pavolonis, M., Kuhn, T., Gurka, J., Liu, P., and Cermak, J.: A review on ice fog measurements and modeling, Atmospheric Research, 151, 2–19, https://doi.org/https://doi.org/10.1016/j.atmosres.2014.04.014, sixth International Conference on Fog, Fog Collection and Dew, 2015.

Gultepe, I., Heymsfield, A. J., Gallagher, M., Ickes, L., and Baumgardner, D.: Ice Fog: The Current State of Knowledge and Future Challenges, Meteorological Monographs, 58, 4.1 – 4.24, https://doi.org/10.1175/AMSMONOGRAPHS-D-17-0002.1, 2017.

Heymsfield, A. J. and Sabin, R. M.: Cirrus Crystal Nucleation by Homogeneous Freezing of Solution Droplets, Journal of Atmospheric Sciences, 46, 2252 – 2264, https://doi.org/10.1175/1520-0469(1989)046<2252:CCNBHF>2.0.CO;2, 1989.

Heymsfield, A. J., Krämer, M., Luebke, A., Brown, P., Cziczo, D. J., Franklin, C., Lawson, P., Lohmann, U., McFarquhar, G., Ulanowski, Z., and Tricht, K. V.: Cirrus Clouds, Meteorological Monographs, 58, 2.1 – 2.26, https://doi.org/10.1175/AMSMONOGRAPHS-D-16-0010.1, 2017.

Izett, J. G. and van de Wiel, B. J. H.: Why Does Fog Deepen? An Analytical Perspective, Atmosphere, 11, https://doi.org/10.3390/atmos11080865, 2020.

Jensen, E. J., Ueyama, R., Pfister, L., Bui, T. V., Alexander, M. J., Podglajen, A., Hertzog, A., Woods, S., Lawson, R. P., Kim, J.-E., and Schoeberl, M. R.: High-frequency gravity waves and homogeneous ice nucleation in tropical tropopause layer cirrus, Geophysical Research Letters, 43, 6629–6635, https://doi.org/https://doi.org/10.1002/2016GL069426, 2016.

Kikuchi, K.: Observations of Concentration of Ice Nuclei at Syowa Station, Antarctica, Journal of the Meteorological Society of Japan. Ser. II, 49, 20–31, https://doi.org/10.2151/jmsj1965.49.1_20, 1971.

Kikuchi, K.: Sintering Phenomenon of Frozen Cloud Particles Observed at Syowa Station, Antarctica, Journal of the Meteorological Society of Japan. Ser. II, 50, 131–135, https://doi.org/10.2151/jmsj1965.50.2_131, 1972.

435   Koop, T., Luo, B., Tsias, A., and Peter, T.: Water activity as the determinant for homogeneous ice nucleation in aqueous solutions, Nature, 406, 611–614, 2000.

Kärcher, B. and Burkhardt, U.: A cirrus cloud scheme for general circulation models, Quarterly Journal of the Royal Meteorological Society, 134, 1439–1461, https://doi.org/https://doi.org/10.1002/qj.301, 2008.

Kärcher, B. and Lohmann, U.: A parameterization of cirrus cloud formation: Heterogeneous freezing, Journal of Geophysical Research:
440   Atmospheres, 108, https://doi.org/https://doi.org/10.1029/2002JD003220, 2003.

Lanconelli, C., Busetto, M., Dutton, E. G., König-Langlo, G., Maturilli, M., Sieger, R., Vitale, V., and Yamanouchi, T.: Polar Baseline surface radiation measurements during the International Polar Year 2007-2009, Earth Syst Sci Data Discuss, 3, 1–8, doi:10.5194/essd-3-1-2011, 2011.

Libois, Q., Picard, G., Arnaud, L., Morin, S., and Brun, E.: Modeling the impact of snow drift on the decameter-scale variability of snow
445   properties on the Antarctic Plateau, J Geophys Res Atmos, 119, 662–681, doi:10.1002/2014JD022361., 2014.

Marcolli, C.: Deposition nucleation viewed as homogeneous or immersion freezing in pores and cavities, Atmospheric Chemistry and Physics, 14, 2071–2104, https://doi.org/10.5194/acp-14-2071-2014, 2014.

Murphy, D. M. and Koop, T.: Review of the vapour pressures of ice and supercooled water for atmospheric applications, Quarterly Journal of the Royal Meteorological Society, 131, 1539–1565, https://doi.org/https://doi.org/10.1256/qj.04.94, 2005.

450   Nachbar, M., Duft, D., and Leisner, T.: The vapor pressure of liquid and solid water phases at conditions relevant to the atmosphere, The Journal of Chemical Physics, 151, 064 504, https://doi.org/10.1063/1.5100364, 2019.

Neis, P., Smit, H. G. J., Krämer, M., Spelten, N., and Petzold, A.: Evaluation of the MOZAIC Capacitive Hygrometer during the airborne field study CIRRUS-III, Atmospheric Measurement Techniques, 8, 1233–1243, https://doi.org/10.5194/amt-8-1233-2015, 2015.

Palchetti, L., Bianchini, G., Natale, G. D., and Guasta, M. D.: Far-Infrared Radiative Properties of Water Vapor and Clouds in Antarctica,
455   Bulletin of the American Meteorological Society, 96, 1505–1518, https://doi.org/10.1175/BAMS-D-13-00286.1, 2015.

Ren, C. and Mackenzie, A. R.: Cirrus parametrization and the role of ice nuclei, Quarterly Journal of the Royal Meteorological Society, 131, 1585–1605, https://doi.org/https://doi.org/10.1256/qj.04.126, 2005.

Ricaud, P., Genthon, C., Durand, P., Attié, J., Carminati, F., Canut, G., Vanacker, J., Moggio, L., Courcoux, Y., Pellegrini, A., and Rose, T.: Summer to winter diurnal variabilities of temperature and water vapour in the lowermost troposphere as observed by HAMSTRAD over
460   Dome C, Antarctica,, Boundary-Layer Meteorol, 143, 227–259, 2012.

Ricaud, P., Bazile, E., del Guasta, M., Lanconelli, C., Grigioni, P., and Mahjoub, A.: Genesis of diamond dust, ice fog and thick cloud episodes observed and modelled above Dome C, Antarctica, Atmospheric Chemistry and Physics, 17, 5221–5237, https://doi.org/10.5194/acp-17-5221-2017, 2017.

Ricaud, P., Del Guasta, M., Bazile, E., Azouz, N., Lupi, A., Durand, P., Attié, J.-L., Veron, D., Guidard, V., and Grigioni, P.: Supercooled
465   liquid water cloud observed, analysed, and modelled at the top of the planetary boundary layer above Dome C, Antarctica, Atmospheric Chemistry and Physics, 20, 4167–4191, https://doi.org/10.5194/acp-20-4167-2020, 2020.

Rowe, P. M., Walden, V. P., Brandt, R. E., Town, M. S., Hudson, S. R., and Neshyba, S.: Evaluation of Temperature-Dependent Complex Refractive Indices of Supercooled Liquid Water Using Downwelling Radiance and In-Situ Cloud Measurements at South Pole, Journal of Geophysical Research: Atmospheres, 127, e2021JD035 182, https://doi.org/https://doi.org/10.1029/2021JD035182, 2022.

470   Santachiara, G., Belosi, F., and Prodi, F.: Ice crystal precipitation at Dome C site (East Antarctica), Atmospheric Research, 167, 108–117, https://doi.org/https://doi.org/10.1016/j.atmosres.2015.08.006, 2016.

Silber, I., Fridlind, A. M., Verlinde, J., Ackerman, A. S., Chen, Y.-S., Bromwich, D. H., Wang, S.-H., Cadeddu, M., and Eloranta, E. W.: Persistent Supercooled Drizzle at Temperatures Below -25^oC Observed at McMurdo Station, Antarctica, Journal of Geophysical Research: Atmospheres, 124, 10 878–10 895, https://doi.org/10.1029/2019JD030882, 2019.

475   Stull, R. B.: An Introduction to Boundary Layer Meteorology, Kluver, Boston, 1990.

Tomasi, C., Petkov, B. H., and Benedetti, E.: Annual cycles of pressure, temperature, absolute humidity and precipitable water from the radiosoundings performed at Dome C, Antarctica, over the 2005–2009 period, Antarctic Science, 24, 637–658, https://doi.org/10.1017/S0954102012000405, 2012.

van de Wiel, B. J. H., Vignon, E., Baas, P., van Hooijdonk, I. G. S., van der Linden, S. J. A., van Hooft, J. A., Bosveld, F. C., de Roode,
480   S. R., Moene, A. F., and Genthon, C.: Regime transition in near-surface temperature inversions: a conceptual model, J Atmos Sci, 74, 1057–1073, doi:10.1175/JAS-D-16-0180.1, 2017.

van der Linden, S. J., Edwards, J. M., van Heerwaarden, C. C., Vignon, E., Genthon, C., Petenko, I., Baas, P., Jonker, H. J., and van de Wiel, B. J.: Large-eddy simulations of the steady wintertime Antarctic boundary layer, Boundary-Layer Meteorology, 173, 165–192, https://doi.org/10.1007/s10546-019-00461-4, 2019.

485   Vignon, E., Genthon, C., Barral, H., Amory, C., Picard, G., Gallée, H., Casasanta, G., and Argentini, S.: Momentum and heat flux parametrization at Dome C, Antarctica: a sensitivity study, Boundary-Layer Meteorol, 162, 341–367, doi: 10.1007/s10546-016-0192-3, 2016.

Vignon, E., van de Wiel, B. J. H., van Hooijdonk, I. G. S., Genthon, C., van der Linden, S. J. A., van Hooft, J. A., Baas, P., Maurel, W., Traullé, O., and Casasanta, G.: Stable Boundary Layer regimes at Dome C, Antarctica: observation and analysis, Q J R Meteorol Soc, 143, 1241–1253, doi:10.1002/qj.2998, 2017.